

1      **Multichannel Analysis of Surface Waves (MASW) for the**  
2      **internal characterisation of the Flüela rock glacier:**  
3      **overcoming the limitations of seismic refraction tomography**

4      Ilaria Barone<sup>1</sup>, Alexander Bast<sup>2,3</sup>, Mirko Pavoni<sup>1</sup>, Steven Javier Gaona Torres<sup>1</sup>, Luca Peruzzo<sup>1</sup>  
5      and Jacopo Boaga<sup>1</sup>

6      <sup>1</sup> Department of Geosciences, University of Padova, Padua, Italy

7      <sup>2</sup> WSL Institute for Snow and Avalanche Research SLF, Permafrost Research Group, Davos Dorf, Switzerland

8      <sup>3</sup> Climate Change, Extremes and Natural Hazards in Alpine Regions Research Center CERC, Davos Dorf,  
9      Switzerland

10     *Correspondence to:* Ilaria Barone ([ilaria.barone@unipd.it](mailto:ilaria.barone@unipd.it)) and Mirko Pavoni ([mirko.pavoni@unipd.it](mailto:mirko.pavoni@unipd.it))

11     **Abstract.** A multi-method geophysical campaign was carried out to characterize the subsurface of the Flüela rock  
12    glacier in Grisons, Switzerland, using electrical resistivity tomography (ERT), seismic refraction tomography  
13    (SRT), and multichannel analysis of surface waves (MASW). Surface-wave analysis is not commonly applied in  
14    mountain permafrost environments, although it can be used on any dataset acquired for conventional SRT when  
15    low-frequency geophones are employed. Here, we show that the MASW method can be effectively used to  
16    highlight the presence of an ice-bearing layer, thereby overcoming potential limitations of conventional SRT in  
17    these environments, such as noisy first arrivals, attenuation effects, and velocity inversions at depth. Our results  
18    are corroborated by synthetic ERT and full-wave seismic modelling, which independently support our subsurface  
19    interpretation.

20

21     Keywords: multichannel analysis of surface waves (MASW); electrical resistivity tomography (ERT); seismic  
22    refraction tomography (SRT); mountain permafrost hydrology; rock glacier hydrology; ground ice content.

23     **1 Introduction**

24     The warming and degradation of European mountain permafrost (PERMOS, 2020; Noetzli et al., 2024) facilitates  
25    the formation and dynamics of alpine mass movements such as rock falls, landslides or debris flows (Arenson and  
26    Jakob, 2014; Kofler et al., 2021; Bast et al., 2024a; Jacquemart et al., 2024), and hence, may impact human safety  
27    and infrastructure (Arenson and Jakob, 2017; Duvillard et al., 2019). Consequently, in densely populated  
28    mountain regions such as the European Alps, there is a significant demand for reliable tools to map and  
29    characterise permafrost environments, accurately assess associated risks, and apply practical solutions for the  
30    construction and maintenance of durable infrastructure (e.g., Bommer et al., 2010).

31     Rock glaciers are common, widespread, often tongue-shaped debris landforms found in periglacial mountain  
32    environments containing ice, rocks, air and water (Kellerer-Pirklbauer et al., 2024; Haeberli et al., 2006;

33 RGIK, 2022). They form in the deposition zones of snow avalanches and rock fall (Kenner et al. 2019) and  
34 develop over centuries to millennia (Krainer et al., 2015; Haeberli et al., 1999) due to past or ongoing creep  
35 (RGIK, 2022), resulting from internal deformation within the ground ice and shearing at distinct horizons  
36 (Arenson et al., 2002; Cicoira et al., 2021). In the past two decades, the creep rate of rock glaciers has generally  
37 increased, and this is often linked to climate change (Kellerer-Pirkelbauer et al., 2024; PERMOS 2020, Hu et al.  
38 2025).

39 Rock glaciers have primarily been studied from geomorphological, climatic, and kinematic perspectives, with less  
40 focus on their hydrological aspects (e.g., Bast et al., 2024b; Cicoira et al., 2019; Haeberli et al., 2006; Hu et al.,  
41 2025; Kellerer-Pirkelbauer et al., 2024; Kenner et al., 2020), as also highlighted by recent reviews by Arenson et  
42 al. (2022) and Jones et al. (2019). This gap in understanding arises because of the complexity of the distribution  
43 of ice and water in rock glaciers. The relation between rock glacier kinematics and their hydrology is also complex,  
44 influenced by factors such as variable surface cover and groundwater flow, which affect infiltration rates, heat  
45 transfer and reaction times (Arenson et al., 2022). Nevertheless, understanding rock glacier hydrology is essential  
46 to comprehend rock glacier velocities, i.e. kinematics, and their potential impacts on alpine mass movements.

47 Water can exist within rock glaciers as seasonally frozen in the active layer, as perennially frozen ice in the  
48 permafrost body, or perennially unfrozen in liquid form in taliks. Permafrost primarily influences water flow paths  
49 by acting as a physical barrier that restricts movement (Arenson et al., 2022). Conceptual models (Giardino et al.,  
50 1992), alongside geochemical (Krainer and Mostler, 2002; Krainer et al., 2007) and geophysical studies (Pavoni  
51 et al., 2023a), suggest that a continuous ice-rich frozen layer functions as an aquiclude, separating supra-  
52 permafrost flow caused by snow and ice melt, as well as precipitation, from a deeper sub-permafrost flow (Jones  
53 et al. 2019). However, the stratigraphy and the bedrock under rock glaciers are often very heterogeneous over  
54 short distances, complicating the hydrology (Bast et al., 2024b; Boaga et al., 2020). The thermal state of the  
55 ground also plays a critical role, as liquid water can exist below 0°C due to factors such as water salinity, high  
56 clay content, or pressure (Arenson et al., 2022; Arenson and Sego, 2006; Bast et al., 2024b; Williams, 1964). This  
57 affects the unfrozen water content and hydraulic conductivity and may lead to intra-permafrost flow, confined  
58 water layers or water pockets. Furthermore, heat transport by flowing water can facilitate thawing in specific  
59 regions, for instance, leading to the development of taliks (Arenson et al., 2022).

60 Although boreholes provide the most accurate information on the internal structure of rock glaciers (Arenson et  
61 al., 2002) and allow the monitoring of subsurface properties through specialised sensors such as high-accuracy  
62 piezoresistive level probes with temperature sensors or inclinometers (Bast et al., 2024b; Phillips et al., 2023;  
63 Arenson et al., 2002), they only offer point data, they are expensive and are challenging to install in high mountain  
64 environments. Geophysical methods are, therefore, often used to achieve a more detailed characterisation of the  
65 subsurface and a spatial extent (e.g., Scott et al., 1990; Hauck and Kneisel, 2008).

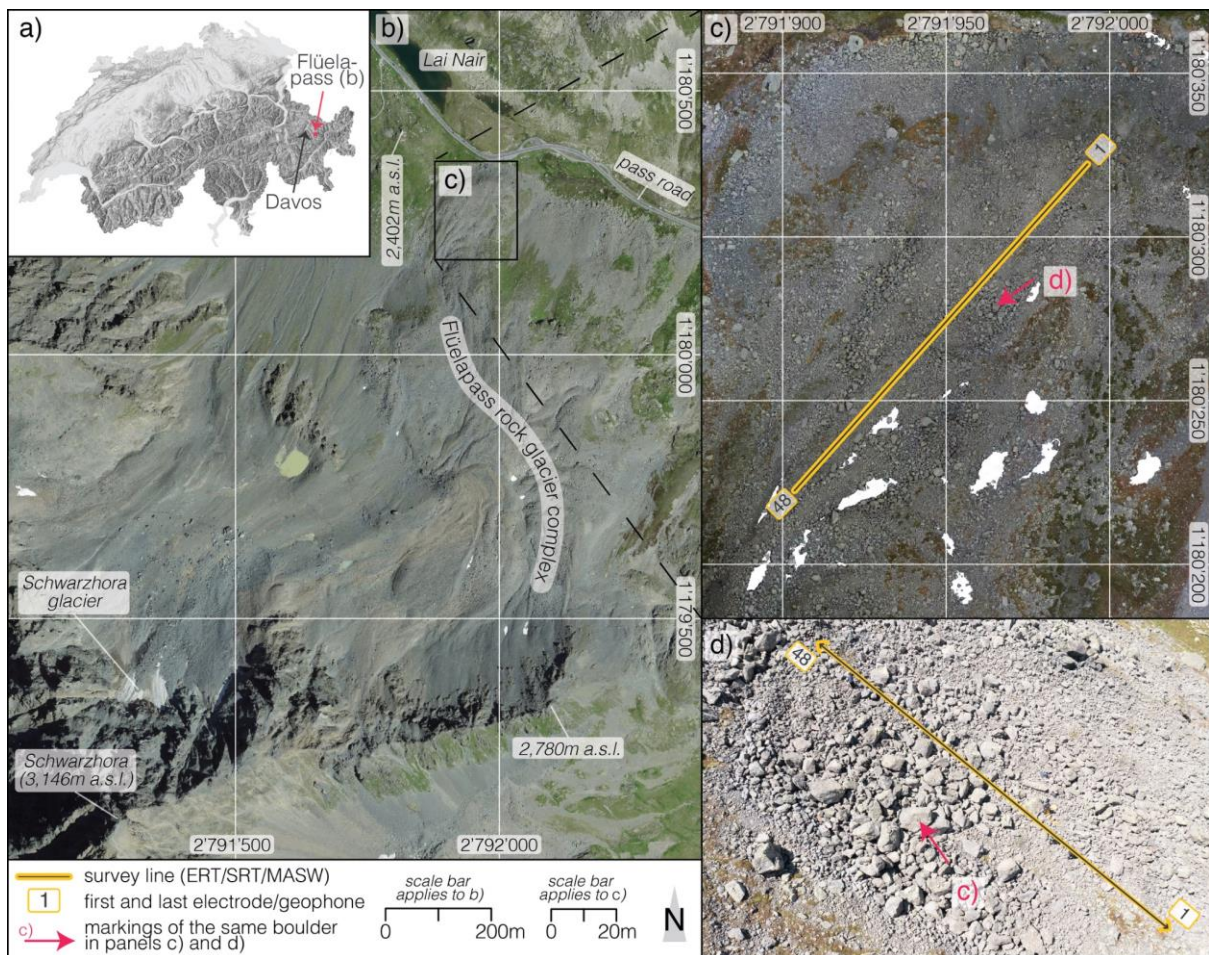
66 Among the different geophysical techniques, electrical resistivity tomography (ERT) and seismic refraction  
67 tomography (SRT) methods are widely used to estimate the structure and internal composition of rock glaciers  
68 (Wagner et al., 2019; Pavoni et al., 2023b; Hauck et al., 2011; de Pasquale et al., 2022). Single-station passive  
69 seismic methods such as HVSR (Horizontal-to-Vertical Spectral Ratio) are also increasingly popular for  
70 permafrost characterization and monitoring (Kula et al. 2018), including in rock glacier environments (Guillemot  
71 et al. 2020, Guillemot et al. 2021, Colombero et al. 2025). Among the advantages of passive seismic methods  
72 there is the simplified logistics, which is counterbalanced by the point-station character of the measurement and

73 the lack of high frequencies, resulting in a reduced sensitivity in the very near surface. On the other hand, the  
74 multichannel analysis of surface waves (MASW; Park et al., 1999), commonly applied for civil engineering  
75 purposes (Park et al., 2018; Olafsdottir et al., 2024) and recently used in permafrost studies in Arctic regions  
76 (Glazer et al. 2020, Liu et al. 2022, Tourei et al. 2024), has rarely been applied in mountain permafrost  
77 environments (Guillemot et al., 2021; Kuehn et al., 2024). Nevertheless, a seismic shot gather acquired with low-  
78 frequency vertical geophones (e.g., with a 4.5 Hz natural frequency) not only records the first arrivals of direct  
79 and refracted P-waves but also Rayleigh waves, whose propagation is mainly sensitive to S-wave velocities (Vs).  
80 Thus, the application of the MASW method can potentially allow the retrieval of a Vs profile (Socco et al., 2010),  
81 complementing the SRT method, which typically focuses on P-wave velocities (Vp). The MASW method offers  
82 several advantages over the SRT technique: i) it can reveal velocity inversions in the subsurface, such as a lower  
83 velocity layer between two higher velocity layers, ii) the retrieved S-wave velocities are insensitive to the liquid  
84 phase present in the medium, and iii) it can provide quantitative information regarding the subsurface mechanical  
85 properties like the shear modulus and Young's modulus, for geotechnical characterisation (Park et al., 2007).  
86 In this study, we applied the MASW method along a seismic line acquired next to an ERT line at the Flüela rock  
87 glacier, Grisons, Switzerland. ERT suggests the presence of an ice-bearing layer in the upper part of the rock  
88 glacier tongue, which disappears towards the front. The SRT analysis clearly detects the basal bedrock but  
89 surprisingly does not reveal the typical P-wave velocities of the ice-bearing layer. In fact, the SRT results indicate  
90 Vp values typical of liquid water, thereby masking the presence of the ice-bearing layer. In contrast, the Vs models  
91 obtained from the MASW results are in very good agreement with the ERT findings. We therefore hypothesise  
92 that the difficulties encountered in the SRT analysis in detecting the ice-bearing layer are due to the presence of  
93 a thin water-saturated sediment layer overlying the ice-bearing layer (supra-permafrost flow), which would inhibit  
94 P-wave propagation, as well as relatively high picking uncertainties. To support our hypothesis, we performed  
95 both full-wave seismic forward modelling, producing synthetic shot gathers for comparison of surface-wave  
96 dispersion and P-wave first-arrival times, and synthetic ERT modelling to evaluate the capacity of the adopted  
97 ERT array to resolve the thin water-saturated layer above the permafrost.

## 98 **2 Study site and data acquisition**

99  
100 The lower lobe of the Flüelapass rock glacier complex (referred to here as the Flüela rock glacier; 46.746° N,  
101 9.951° E) is located in the Eastern Swiss Alps, next to the Flüelapass road in the Community of Zernez, Grisons,  
102 at the top of the mountain pass (Figs. 1a and 1b). The active rock glacier, ranging from 2380-2500 m asl., is  
103 nourished by the surrounding steep rock walls, which are composed of amphibolite and paragneiss  
104 (Bast et al., 2025). The lower investigated tongue of the rock glacier (Fig. 1c) creeps downwards with surface  
105 velocities ranging between ~ 10 and ~ 30 cm/year (R. Kenner, SLF, personal communication, based on annual  
106 terrestrial laser scans, 2024). The surface material consists of rock debris and boulders of various sizes, along with  
107 smaller isolated patches of finer sediments and sparse vegetation (Figs. 1c and 1d).  
108 A first study of the Flüela rock glacier by Haeberli (1975) applied refraction seismics to investigate the presence  
109 of ground ice. The seismic profiles obtained indicated permafrost at around 10 m depth in the rock glacier front  
110 and ice-rich ground below approximately 4 m towards the central lower area of the rock glacier. More recent

111 geophysical research by Boaga et al. (2024) and Bast et al. (2025) confirmed the presence of the ice-bearing layer.  
 112 Research on permafrost distribution and evolution at the Flüelapass primarily concentrated on a talus slope located  
 113 approximately 500 m west-northwest, where two boreholes were drilled in 2002 (Lerjen et al., 2003; Phillips et  
 114 al., 2009; Kenner et al., 2017). As for the lower tongue investigated here, no borehole information is available.  
 115



116  
 117 **Figure 1:** (a) Location of the Flüela rock glacier complex in Switzerland. (b) Aerial image of the Flüelapass featuring  
 118 the Flüela rock glacier complex, with markers for orientation (summit, lake, road) and elevation points. (c) A zoomed-  
 119 in drone ortho mosaic (flight date 28 June 2023) of the investigated lower lobe of the rock glacier complex, highlighting  
 120 the survey line (electrical resistivity and seismic data, yellow-grey line). The red arrow indicates the same boulder as  
 121 in the oblique drone image (d). The drone image reveals the coarse and rough surface within the middle section of the  
 122 survey line (please note that the survey line extends further NW and SW). Basemaps in a) SwissAlti3D multidirectional  
 123 hillshade and b) SwissImage (flight year 2022) are provided by swisstopo (<https://map.geo.admin.ch>). Note that the  
 124 legend and North arrow applies to all map sections (a-c).

125 On 03 August 2024, we collected both electrical resistivity tomography (ERT) and seismic data on the rock  
 126 glacier. The measurements were collected along a line of approximately 133 m in the middle of the lobe (Figs. 1c  
 127 and 1d). For data collection, we used 48 electrodes for the ERT and 48 geophones for the seismics, with a spacing  
 128 of 3 m. We measured all electrode/geophone positions with a Stonex S800 GNSS instrument (Stonex, Paderno  
 129 Dugnano, Italy; [www.stonex.it](http://www.stonex.it)) to obtain a detailed topographic profile along the survey line.

130 The ERT dataset was collected with a Syscal Pro Switch 48 resistivity meter (IRIS Instruments, Orléans, France;  
131 [www.iris-instruments.com](http://www.iris-instruments.com)). This was done with a dipole-dipole multi-skip acquisition scheme  
132 (Pavoni et al., 2023a), with reciprocal measurements and stacking ranging from 3 to 6 (Day-Lewis et al., 2008),  
133 for a total of 3542 measured data points. To ensure a good galvanic coupling, i.e., optimal contact resistances, and  
134 to obtain a high-quality dataset (Pavoni et al., 2022), conductive textile sachets, wet with salt water, were used as  
135 electrodes (Buckel et al., 2023; Bast et al., 2025).

136 The seismic data were collected with two Geode seismographs (Geometrics, San Jose, USA;  
137 <http://www.geometrics.com>), using vertical low-frequency geophones with a natural frequency of 4.5 Hz and a  
138 20 kg sledgehammer as a seismic source. The source was moved from the first to the last geophone with a distance  
139 of six metres between each position, resulting in a total of 24 acquisition positions. At each position, the shot was  
140 repeated twice to stack the seismograms and enhance the signal-to-noise ratio.

### 141 3 MASW Method

142 Surface waves are seismic waves that travel along the Earth's surface, characterised primarily by dispersion, i.e.,  
143 different frequencies propagate at different velocities (Everett, 2013). By analysing surface wave dispersion, it is  
144 possible to infer different mechanical properties of the medium through which the surface waves propagate (Socco  
145 et al., 2010). The depth of investigation of surface waves is associated with the seismic wavelength; a general rule  
146 of thumb is to consider one-third to one-half of the seismic wavelength of the lowest frequency component as the  
147 maximum penetration depth (Foti et al., 2015). Surface waves are also characterised by multi-modal propagation,  
148 meaning they can propagate in multiple modes simultaneously, including the fundamental mode and higher-order  
149 modes. The fundamental mode is the simplest form of wave propagation, with higher sensitivity near the surface,  
150 typically showing lower propagation velocities and higher amplitudes. Higher-order modes involve more complex  
151 sensitivity patterns with depth, can penetrate deeper layers, and usually exhibit higher velocities and lower  
152 amplitudes. However, the energy distribution of surface waves over different modes strongly depends on the  
153 subsurface conditions, and if higher modes with significant amplitude are present, special attention must be  
154 devoted to identifying the different modes (Boaga et al., 2013).

155 Surface wave analysis allows the retrieval of the dispersion relation (phase/group velocity versus frequency). In  
156 particular, the Multichannel Analysis of Surface Waves (MASW; Park et al., 1999) uses linear arrays to record  
157 the surface wave propagation from an active source in the time-space domain (seismogram). The acquisition setup  
158 is identical to SRT, but low-frequency geophones, having typically a natural frequency of 4.5 Hz, are essential  
159 for MASW surveys. The seismogram is converted into a frequency-wavenumber (f-k) or frequency-velocity (f-v)  
160 spectrum, where the energy maxima corresponding to the different modes are picked. Depth inversion is finally  
161 needed to retrieve a 1D Vs profile. Inversion is a non-linear ill-posed problem that can be solved deterministically  
162 using the linearized iterative least-squares approach (Herrmann, 1987), or with a stochastic search method, such  
163 as the neighbourhood algorithm (Sambridge, 1999). In both cases, some preliminary information is needed to  
164 define the starting model (deterministic approach) or the parameter space (stochastic approach).

165 The MASW method assumes homogeneous lateral conditions under the recording array. This condition is hardly  
166 met in nature, and when strong lateral heterogeneities are present, the complexity of the resulting spectra could  
167 challenge the picking process. For this reason, MASW is sometimes applied using moving windows. In this case,  
168 a quasi-2D Vs profile is retrieved, and smooth lateral velocity variations can be identified (Bohlen et al., 2004;

169 Boiero and Socco, 2011). The selection of the moving window length is crucial and requires preliminary testing:  
170 a shorter window length causes an increase in lateral resolution but decreases the spectral resolution.

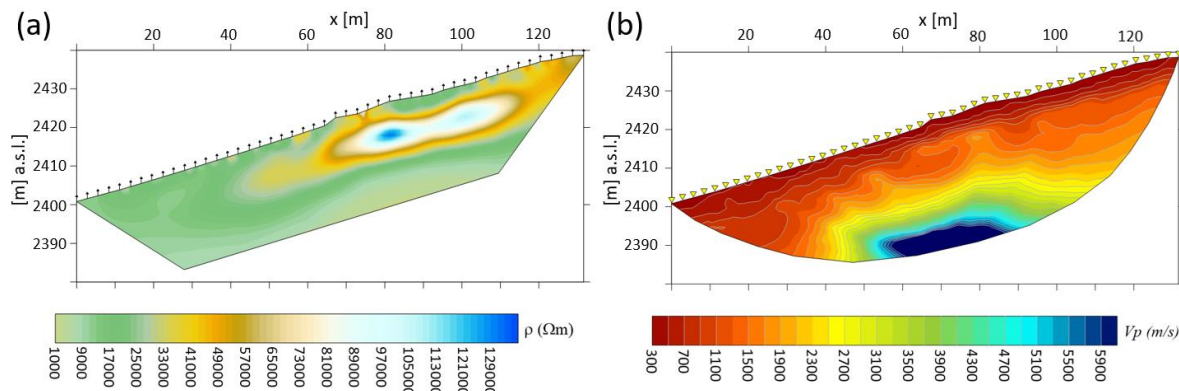
171

172 **4 ERT, SRT and MASW data processing, results and interpretation**

173  
174 **4.1 ERT and SRT**

175  
176 The ERT data processing was conducted using the open-source Python-based software *ResIPy*  
177 (Blanchy et al., 2020), filtering the quadrupoles with reciprocal and stacking errors exceeding 5 %, which was  
178 considered as the expected data error in the inversion modelling (Day-Lewis et al., 2008). This resulted in the  
179 removal of 344 quadrupoles over 1324. The inverted resistivity model (Fig. 2a) was found in two iterations and  
180 with a final RMS (Root-Mean Square) misfit of 1.17.

181 SRT data processing was performed with two open-source tools. Geogiga Front End Express v. 10.0, from  
182 Geogiga Technology Corp. (<https://geogiga.com/products/frontend/>), was used for the picking of first arrivals,  
183 while the C++/Python-based library pyGIMLi (Rücker et al., 2017) was used for data inversion. For each  
184 seismogram, first arrivals were picked multiple times for the same shot and also considering reciprocal shots along  
185 the array, in order to estimate the picking error (1 ms) to be used in the inversion process (Bauer et al., 2010). The  
186 inverted P-wave velocity (Vp) model (Fig. 2b) was obtained after five iterations, with a final  $\chi^2$  (chi-square) misfit  
187 of 1.31.



188  
189 **Figure 2: (a) The inverted ERT section, after two iterations, has an expected data error of 5% and a final RMS misfit**  
190 **of 1.17. The black markers along the surface indicate the positions of the electrodes. (b) The inverted P-wave velocity**  
191 **model (SRT), after five iterations, has a picking error of 1 ms and a final  $\chi^2$  misfit of 1.31. The yellow triangular**  
192 **markers along the surface indicate the positions of the geophones.**

193 In the upper 4 - 5 m of the ground, electrical resistivity values are relatively high (~ 20 kΩm), and Vp values are  
194 particularly low (< 600 m/s). This indicates a highly porous layer composed of blocks and debris with low fine  
195 sediment content. Towards the front of the rock glacier (x < 40 m) and at greater depths, the electrical resistivity  
196 decreases (< 10 kΩm), and the Vp values gradually increase, reaching 1200-1500 m/s at the bottom of the model.  
197 Here, the substrate appears more heterogeneous, consisting of a mix of coarse debris and finer sediments. Towards  
198 the upper section of the rock glacier lobe, at 4 - 5 m depth, resistivities increase (~ 40 kΩm) for 40 m < x < 60 m,  
199 with an even sharper rise to values > 80 kΩm for x > 60 m. These values are typical for an ice-bearing frozen

200 layer (Hauck and Kneisel, 2008; de Pasquale et al., 2022). This layer extends to a depth of 10 - 12 m before  
201 resistivities clearly decrease to a few  $\text{k}\Omega\text{m}$  at the bottom of the model. In the  $\text{Vp}$  model, values increase at greater  
202 depths, with a steep gradient at  $\sim 20$  m depth ( $50 < x < 80$  m), where  $\text{Vp}$  Values reach 6000 m/s, indicating the  
203 bedrock. In the upper part of the section, between 4 - 5 m and 10 - 12 m depth, no typical  $\text{Vp}$  values of an ice-  
204 bearing frozen layer are reached ( $\text{Vp} > 2500$  m/s, Hauck and Kneisel, 2008). Therefore, in this area, the ERT and  
205 SRT results are inconsistent: while the inverted resistivity model clearly indicates an ice-bearing layer, the  $\text{Vp}$   
206 model shows a moderate increase, peaking at  $\text{Vp}$  values  $\sim 1500$  m/s, likely corresponding to a liquid water-  
207 saturated layer.

208

## 209 4.2 MASW

210

211 The MASW analysis was performed using a moving window of 24 channels, striking a balance between spatial  
212 and spectral resolution. An offset-dependent mute was applied to those shot gathers that presented at least one  
213 source bounce as this could significantly impact the subsequent phase measurements. The time of occurrence of  
214 the source bounces was automatically identified through the auto-correlation of the near-offset traces. The mute  
215 was finally applied to the seismogram to mask the source bounce. Each shot gather was then Fourier transformed  
216 in both time and space to obtain the corresponding  $f$ - $k$  spectrum, from which the fundamental mode was manually  
217 picked. The retrieved dispersion curves were depth inverted using *Dinver* (Wathelet, 2008), an open-source tool  
218 included in *Geopsy* (<https://www.geopsy.org/>; last access: 28 February 2025) that performs a stochastic inversion  
219 based on the neighbourhood algorithm (Sambridge, 1999). *Dinver* requires the definition of the model space with  
220 a fixed number of layers. We used a four-layer model and parameterized each layer with a wide range of seismic  
221 velocities and Poisson ratios, while keeping the density constant (Tab. 1). This choice was guided by the  
222 preliminary information we gained from ERT and SRT sections, that would indicate two to three layers, depending  
223 on the presence of permafrost, and a relatively shallow seismic bedrock. *Dinver* generates a multitude of random  
224 models within the model space and calculates for each of these models a dimensionless misfit between observed  
225 and modelled dispersion curves (Whatelet et al., 2004). The final model is characterised by the minimum misfit.

226 **Table 1: Parameter space used for the dispersion curve inversion with the open-source tool *Dinver* (Wathelet, 2008).**

227 **Abbreviations:**  $\text{Vp}$ : P-wave velocities,  $\text{Vs}$ : S-wave velocities,  $\rho$ : density.

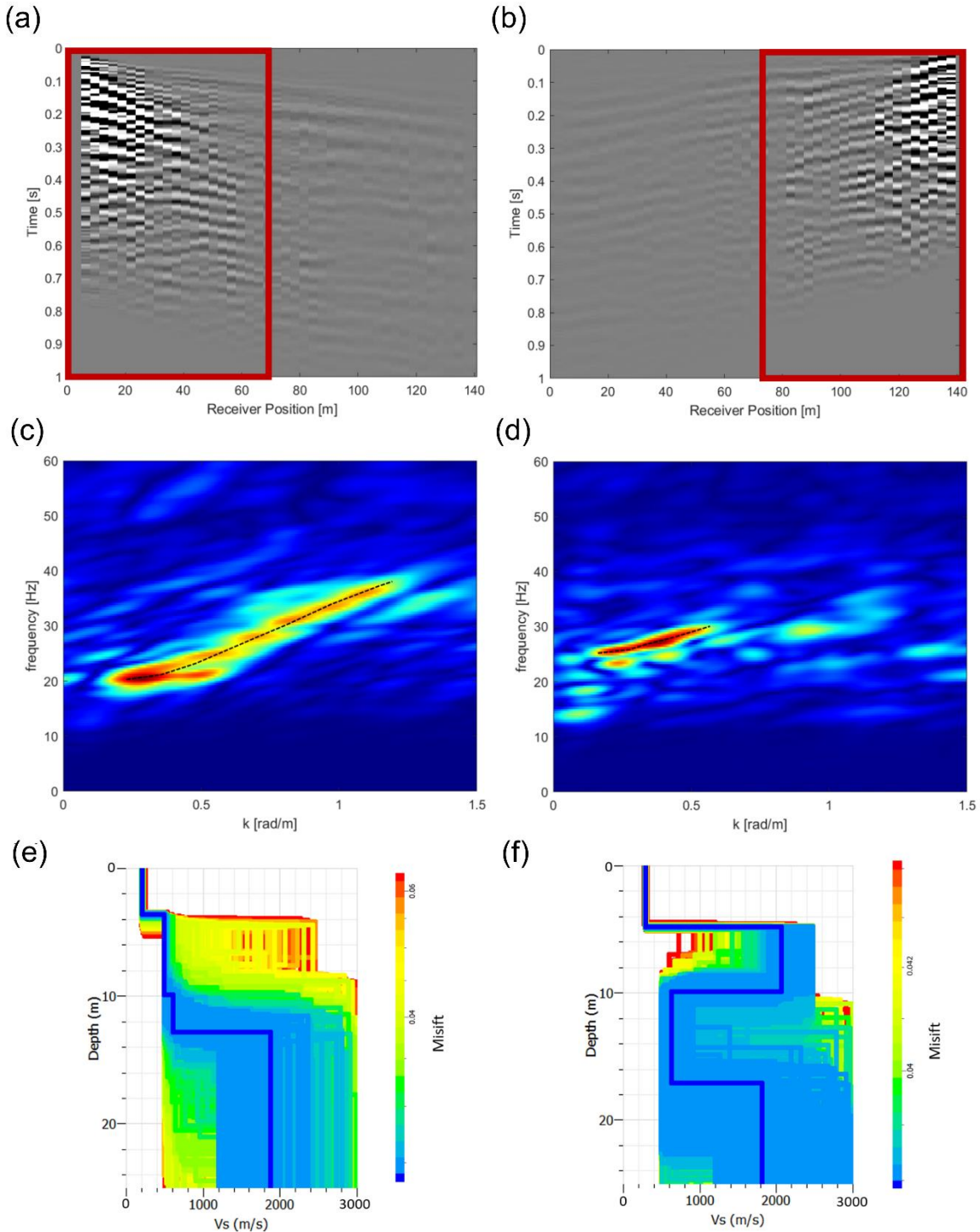
	Thickness [m]	$\text{Vp}$ [m/s]	$\text{Vs}$ [m/s]	Poisson ratio	$\rho$ [kg/m <sup>3</sup> ]
1	2 - 12	400 - 1000	200- 500	0.2 - 0.45	1800
2	2 - 12	800 - 5000	500 - 2500	0.2 - 0.45	2000
3	2 - 12	800 - 5000	500 - 2500	0.2 - 0.45	2000
Bedrock	Infinite	2400 - 6000	1200- 3000	0.2 - 0.45	2200

228

229 Figure 3 shows the results of the picking (Figs. 3c and 3d) and the  $\text{Vs}$  models (Figs. 3e and 3f) derived from the  
230 inversion of two dispersion curves. The first curve refers to a shot placed on the left side and the first 24 geophones  
231 (Fig. 3a), while the second curve relates to a shot on the right side and the last 24 geophones (Fig. 3b). Despite

232 the noisy character of the seismograms, where strong scattering is observed, the f-k spectra show coherent energy  
233 and at least one mode of propagation is clearly recognisable, assumed to be the fundamental mode (Figs. 3c  
234 and 3d). The two spectra show different frequency and wavenumber distributions, indicating different subsurface  
235 conditions. The maximum penetration depth, which is approximately half of the wavelength, can be computed  
236 from the minimum picked frequency, and it is about 15 m. The inversion results reveal a smooth increase of  
237 velocity with depth in the left part of the section, i.e., towards the front of the rock glacier (Fig. 3e), while it clearly  
238 highlights a shallow (5 m depth) high-velocity layer (2000 m/s) on the right side, i.e., the upper part of the rock  
239 glacier (Fig. 3f). The high-velocity layer has a thickness of approximately 5 m. At a depth of 10 m, a clear and  
240 sharp decrease in the velocity is observed. Good convergence is reached in the inversion down to the maximum  
241 sensitivity of 15 m. Below this depth, results should be treated with caution. The lack of convergence manifests  
242 as a wide velocity range with a similar misfit: most models in this depth range are equally plausible. Lower-  
243 frequency data is needed to constrain the inversion at greater depths. It is important to note that the limited  
244 frequency range characterising the picked dispersion curves is partly due to the loss of high frequency from  
245 scattering and partly to the presence of a high-impedance boundary (the top of the bedrock in the left half of the  
246 section and the top of the frozen layer on the right) that likely prevents most of the low-frequency energy from  
247 penetrating below.

248



249

250 Figure 3: (a) Seismogram (grayscale) of the leftmost shot, where the red rectangle indicates the selected receivers for  
 251 analysis. The offset-dependent mute effect is visible after 0.7 s, obscuring the source bounce. (c) Frequency-  
 252 wavenumber (f-k) spectrum of the traces highlighted in (a), with the fundamental mode marked by a black dotted  
 253 curve. The colours represent the seismic energy (low energy in cold colours / high energy in warm colours). (e) Depth  
 254 inversion result of the picked dispersion curve, where colours represent different misfit values; the dark blue bold line  
 255 signifies the final solution model, with a misfit of 0.02416. (b), (d), and (f) correspond to (a), (c), and (e), respectively,  
 256 but for the rightmost shot. In this case, the misfit of the final solution model is 0.03797.

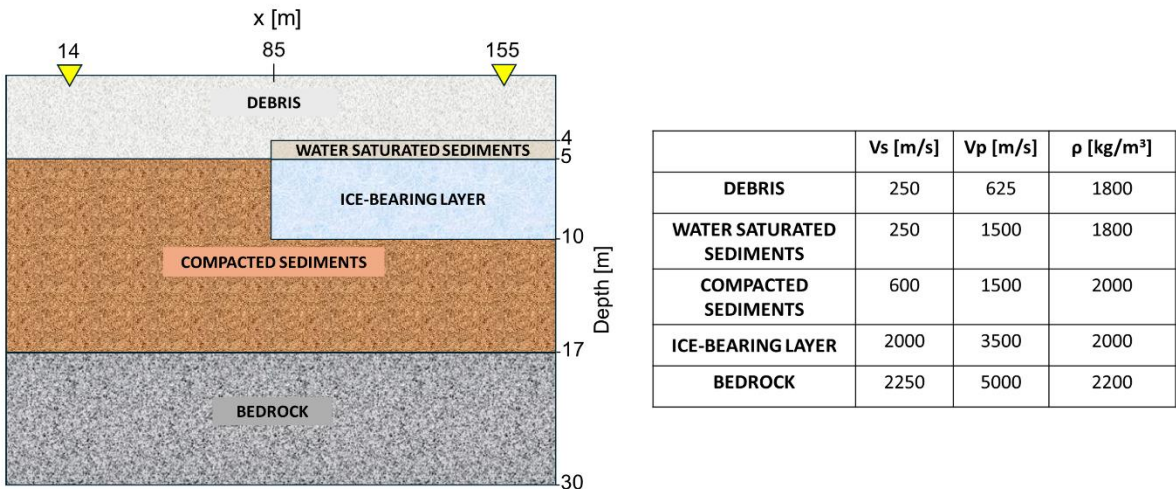
#### 257 4.3 Interpretation

258 The obtained Vs models align well with the inverted resistivity section (Fig. 2a). The Vs values of the shallow  
259 (5 - 10 m depth) high-velocity (2000 m/s) layer observed in the right part of the section (Fig. 3f) are indeed  
260 consistent with the presence of an ice-bearing permafrost layer (Kuehn et al., 2024) that overlies a lower velocity  
261 layer of unfrozen sediments. Conversely, at depths of 5 m and below, the inverted SRT model indicates Vp values  
262 that are too low to support this conclusion, with a maximum value of 1500 m/s, which is characteristic of liquid  
263 water-saturated sediments. This suggests the presence of a supra-permafrost water layer, which can be commonly  
264 found in rock glacier environments where the frozen layer acts as an aquiclude (Krainer et al., 2007;  
265 Pavoni et al., 2023; Arenson et al., 2022, Jones et al., 2019). The ERT model does not resolve the presence of this  
266 (thin) water-saturated layer, likely considering the relatively large spacing of 3 m between the electrodes, nor does  
267 the MASW, which is sensitive to S-waves and thus insensitive to fluids. However, the ~ 1500 m/s P-wave  
268 velocities retrieved by the SRT method may indicate the presence of a (thin) water-saturated layer. In fact, such a  
269 layer may strongly attenuate body wave transmission and mask further impedance contrasts at depth (Pride et al.,  
270 2004). To assess the reliability of our subsurface hypothesis, we conducted both full-wave (FW) seismic  
271 modelling and synthetic ERT modelling (Chapter 5).

## 272 **5 Seismic and ERT Synthetic Modelling**

### 273 **5.1 Seismic synthetic modelling**

274 To verify the reliability of the obtained results, we generated synthetic seismograms based on a simplified  
275 subsurface model derived from the joint interpretation of ERT, SRT and MASW results. Synthetic shot gathers  
276 are compared to the real ones in terms of surface waves and first-arrival times.  
277 Synthetic seismic data are generated using SW4 3.0 (Petersson and Sjögren, 2023), which solves the seismic  
278 wave equations in Cartesian coordinates for 3D heterogeneous media (Sjögren and Petersson, 2012;  
279 Zhang et al., 2021). The conceptual model for the simulation is shown in Fig. 4. The left part of the model is  
280 characterised by three main layers: (i) a 5 m-thick debris layer, (ii) a 12 m-thick layer of more compacted  
281 sediments and (iii) the bedrock. On the right side of the section, we included a 5 m-thick ice-bearing layer, and  
282 we hypothesised a 1 m-thick water-saturated layer above it. This model serves as a simplified representation of  
283 the assumed real subsurface, where clearly, the shape, thickness, and composition of the different layers are not  
284 regular and homogeneous. Moreover, it does not reproduce the small-scale heterogeneities in the model that are  
285 beyond the resolution of our field surveys. However, it represents the main structures highlighted by the MASW,  
286 ERT and SRT results, with the velocity and thickness of the different layers compatible with the results illustrated  
287 in Chapter 4.

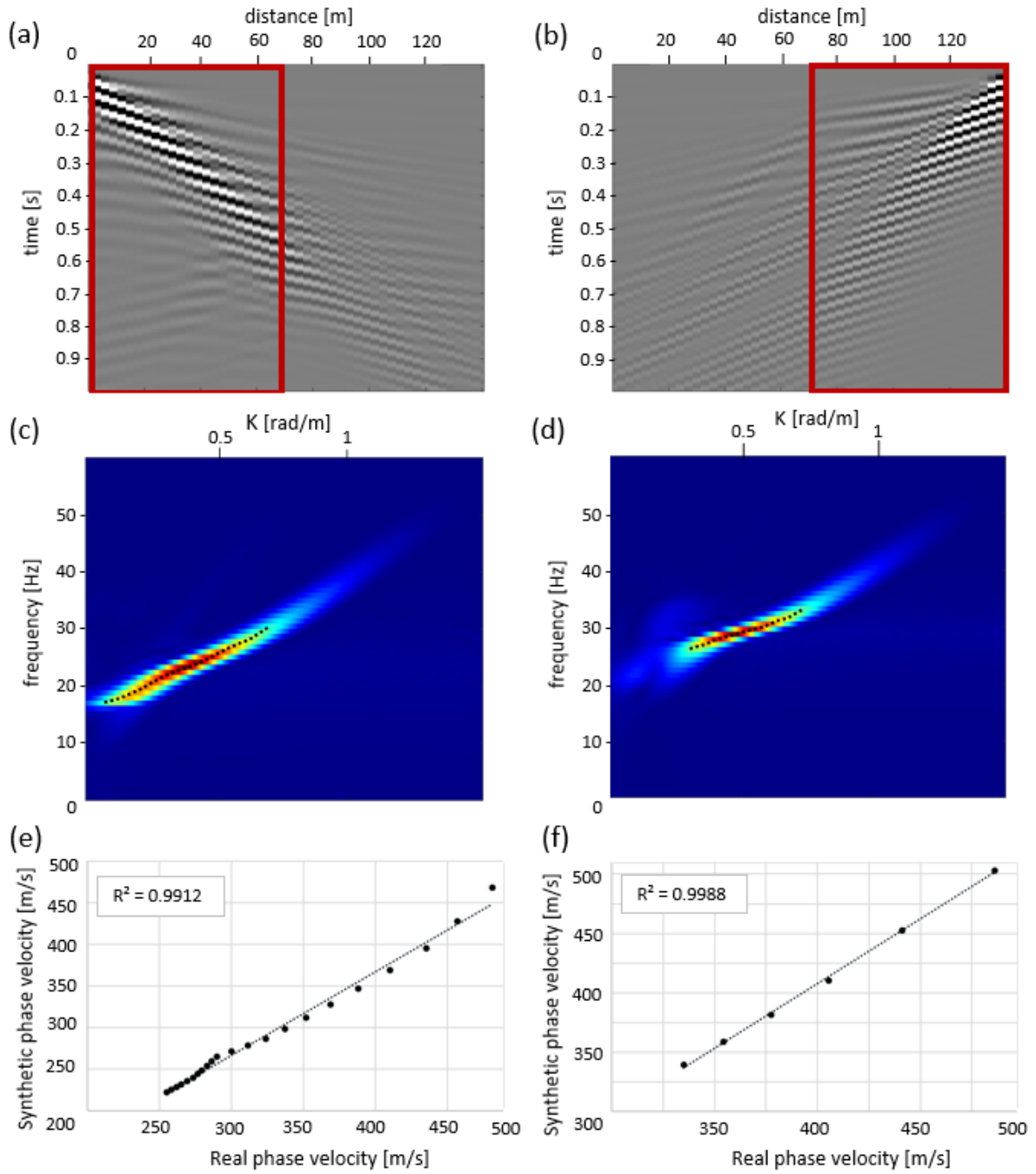


290

291 **Figure 4: Conceptual model used for the synthetic seismic modelling with the SW4 software (Petersson and Sjögren,**  
 292 **2023). The two yellow triangles denote the first and the last geophones in the array. Abbreviations as in Tab. 1.**

293 The simulation domain is 170 x 30 x 30 m in the x, y and z directions. Absorbing boundaries were included in the  
 294 model to prevent the generation of reflections from the model edges, both at its bottom and laterally, while a free  
 295 surface condition was set at the top. The grid step used was 0.5 m, and the time step automatic setting was 0.87  
 296 ms, to comply with the stability criteria. The source was a vertical point load at the surface with central frequency  
 297 and maximum frequency of 15 Hz and 50 Hz, respectively. This choice was again imposed by the numerical  
 298 stability of the forward simulation. An array composed of 48 vertical receivers, with a spacing of 3 m, was placed  
 299 in the middle of the model (14 m  $\leq$  x  $\leq$  155 m, y = 15 m) to reproduce the real case geometry. Two simulations  
 300 were run, corresponding to a shot on the left side of the array at the location of the first receiver and a shot on the  
 301 right side at the last receiver location.

302 Figures 5a and 5b show the synthetic shot gathers as grayscale plots. When compared to Figs. 3a and 3b, it is clear  
 303 how much noisier the field data are compared to the synthetic ones. This is the effect of scattering caused by the  
 304 boulders and coarse debris at the surface of the rock glacier. Consequently, the real f-k spectra (Figs. 3c and 3d)  
 305 are also noisier than the synthetic ones (Figs. 5c and 5d). However, the frequency and wavenumber distribution  
 306 of the fundamental mode in the modelled data is similar to the field observations. This is confirmed by comparing  
 307 the picking of modelled and real spectra (Figs. 5e and 5f). As highlighted in the scatterplots, the phase velocity  
 308 values obtained by sampling the fundamental mode in the synthetic spectra show a high correlation with the  
 309 corresponding values obtained from the field spectra ( $R^2$  value  $\sim 0.99$ ). Note that the comparison was made by  
 310 considering the phase velocity values obtained in the common frequency range in sampling the field spectrum  
 311 (Figs. 3c and 3d) and the synthetic spectrum (Figs. 5c and 5d), i.e., 20-35 Hz on the left side and 25-30 Hz on the  
 312 right side.



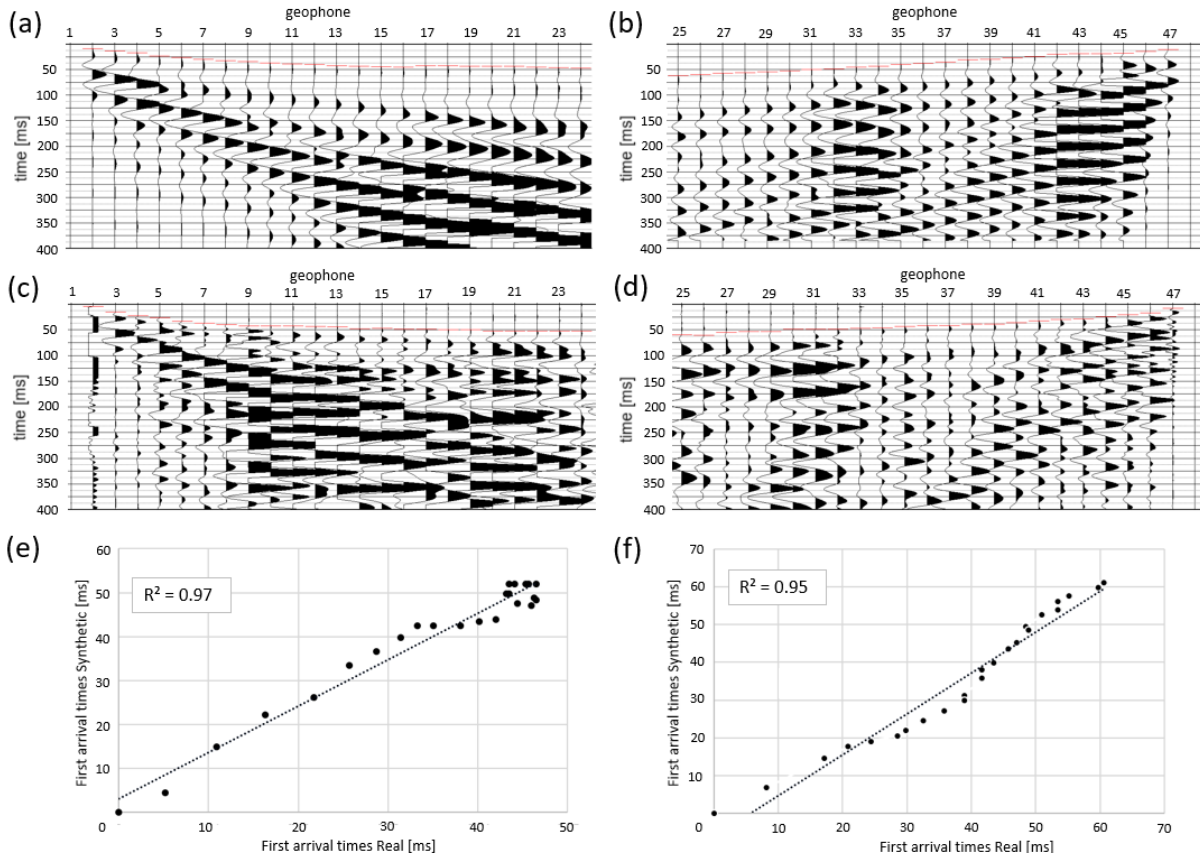
313  
314  
315  
316  
317  
318

Figure 5: (a) Synthetic seismogram (grayscale plot) of the left shot, where the red rectangle indicates the selected receivers for analysis. (c) Frequency-wavenumber (f-k) spectrum of the traces highlighted in (a), with the fundamental mode marked by a black dotted curve. (e) Scatterplot of the phase velocity picking obtained from the real (Fig. 3c) and synthetic spectrum (Fig. 5c). The black dotted lines show a simple linear regression line with corresponding  $R^2$  values. (b), (d), and (f) correspond to (a), (c), and (e), respectively, but for the rightmost shot.

319 First-arrival times picked on the modelled data are highly consistent with the field ones. Figure 6a shows the  
320 synthetic shot gathers (wiggle mode, normalized trace by trace) for sources on the left side of the geophone array,  
321 with the synthetic first arrivals (red lines) closely matching those in the field seismogram (Fig. 6c), as confirmed  
322 by a scatterplot and a high  $R^2$  value (0.97; Fig. 6e). Similarly, for sources on the right side, synthetic (Fig. 6b) and  
323 field (Fig. 6d) shot gathers exhibit comparable first-arrival times (red lines), with a high  $R^2$  value (0.95; Fig. 6f).

324 It is important to notice that synthetic first-arrival traveltimes were not merely modelled kinematically, but with  
 325 a full-wave simulation which takes into account attenuation. In principle, kinematic modelling should generate  
 326 traveltimes whose slopes are compatible with the presence of the ice-bearing layer. Full-wave modelling is  
 327 instead reproducing the attenuation effects of real data. Moreover, the low-frequency content of the source wavelet  
 328 used for the simulation, imposed by the stability criteria, results in a rather low temporal resolution of first arrivals,  
 329 which may generate uncertainties in picking comparable to the observed ones.

330



331

332 **Figure 6: Considering the conceptual model of Fig. 4a, (a) synthetic seismogram of the left shot plotted in wiggle mode**  
 333 **(normalized trace by trace) and the picking (red lines in the traces) of first-arrival times for the first 24 traces; (c)**  
 334 **field seismogram on the left shot plotted in wiggle mode and the picking (red lines in the traces) of first-arrival times for the**  
 335 **first 24 traces; (e) scatterplot of synthetic first-arrival times and field ones for the left shot. The black dotted lines show**  
 336 **a simple linear regression line with corresponding  $R^2$  values. (b), (d), and (f) correspond to (a), (c), and (e), respectively,**  
 337 **but for the rightmost shot.**

338 The good agreement between synthetic and field data regarding surface wave dispersion and first-arrival times,  
 339 demonstrates the validity of the simple conceptual model presented in Fig. 4, which was used for the forward  
 340 simulation. However, slight differences in the synthetic and field picking of the fundamental mode and first-arrival  
 341 times may relate to the simplification of the synthetic model, which could not account for the highly complex  
 342 topography and the heterogeneities of shape, thickness, and composition in the different layers.

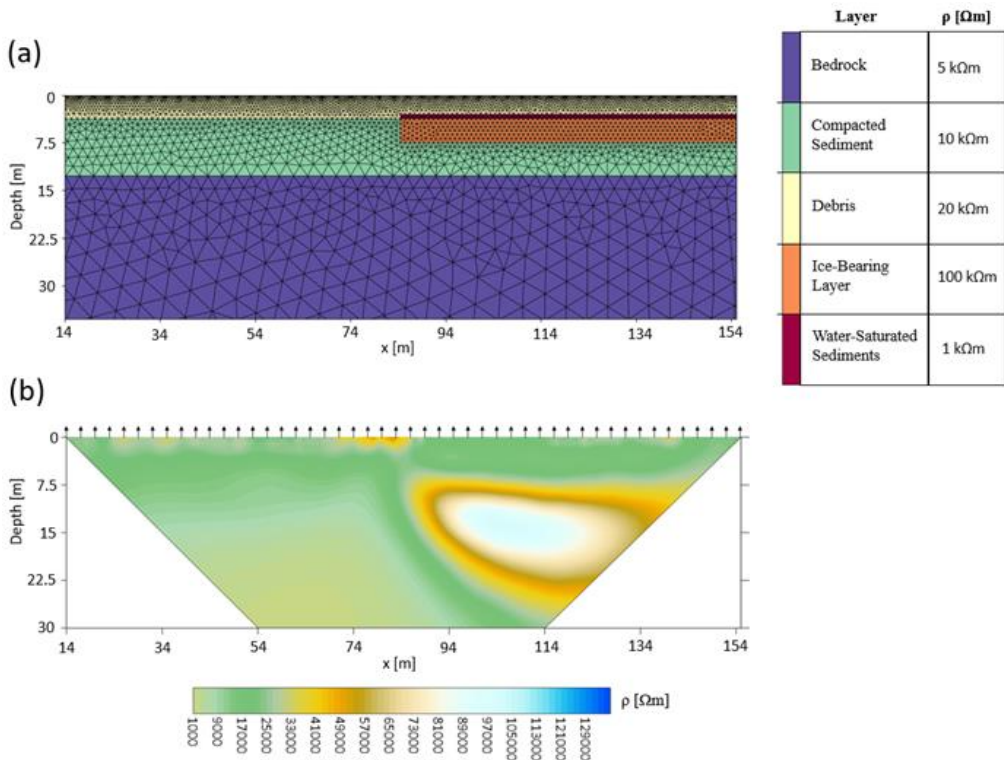
343 **5.2 ERT synthetic modelling**

344 ERT synthetic modelling involves the numerical simulation of the electrical potential distribution in the  
345 subsurface based on a known resistivity model. This process requires solving Poisson's equation, which describes  
346 the behavior of the electric field generated by current injection through electrodes placed on the surface or in  
347 boreholes (Binley & Slater, 2020). In this study, the process was performed using the open-source software ResIPy  
348 (Blanchy et al., 2020) and the objective was to evaluate whether the electrode array and acquisition configuration  
349 used during the measurement campaign at the Flüela rock glacier provided sufficient resolution to detect a thin  
350 layer of water-saturated sediment overlying the permafrost. We hypothesize that this layer may have contributed  
351 to the attenuation of P-wave propagation at depth.

352 The synthetic modelling was based on the subsurface structure shown in Fig. 4, with electrical resistivity values  
353 assigned to each layer according to the inverted resistivity model derived from field data (Fig. 2a). Specifically,  
354 resistivities of 20 kΩ·m, 10 kΩ·m, 5 kΩ·m, and 100 kΩ·m were assigned to the surface debris layer, compact  
355 sediment, bedrock, and frozen layer, respectively (Fig. 7a). A representative value of 1 kΩ·m was assigned to the  
356 water-saturated sediment layer. In rock glacier environments, such layers can exhibit resistivities depending on  
357 factors such as material composition, water chemistry, and temperature. The assigned value is plausible  
358 particularly when the substrate consists of coarse, blocky debris with large pore spaces and low clay content,  
359 which tends to maintain relatively high resistivity even under saturated conditions (Hauck & Vonder Mühll, 2003;  
360 Hilbich et al., 2021). Additionally, if the pore water has low ionic content—as is typical of glacial meltwater—  
361 the resulting resistivity remains relatively high (Hauck, 2002).

362 The synthetic dataset was generated using a dipole–dipole multi-skip acquisition scheme identical to that  
363 employed in the field survey, with an array of 48 electrodes spaced 3 meters apart. A 5% noise level was added  
364 to the synthetic measurements, consistent with the estimated noise in the real dataset. The synthetic data were  
365 then inverted using the same parameters applied to the inversion of the real dataset, resulting in the resistivity  
366 model shown in Fig. 7b. The result does not clearly reveal the presence of the thin water-saturated sediment layer  
367 overlying the frozen layer, confirming that the ERT survey conducted at the Flüela rock glacier site lacked the  
368 resolution and configuration necessary to resolve such a feature. This limitation is likely due to the relatively large  
369 electrode spacing.

370 Compared to the real electrical resistivity model (Fig. 2a), slight deviations can be observed, which can be  
371 attributed to the simplifications adopted in the conceptual model which does not account for the natural  
372 heterogeneity typically encountered in the field, including lateral and vertical variations in layer thickness,  
373 composition, and continuity. As in the seismic synthetic modelling, we assumed laterally homogeneous, planar  
374 layers and excluded surface topography, resulting in an idealized representation intended to enhance the  
375 theoretical detectability of the target layer.



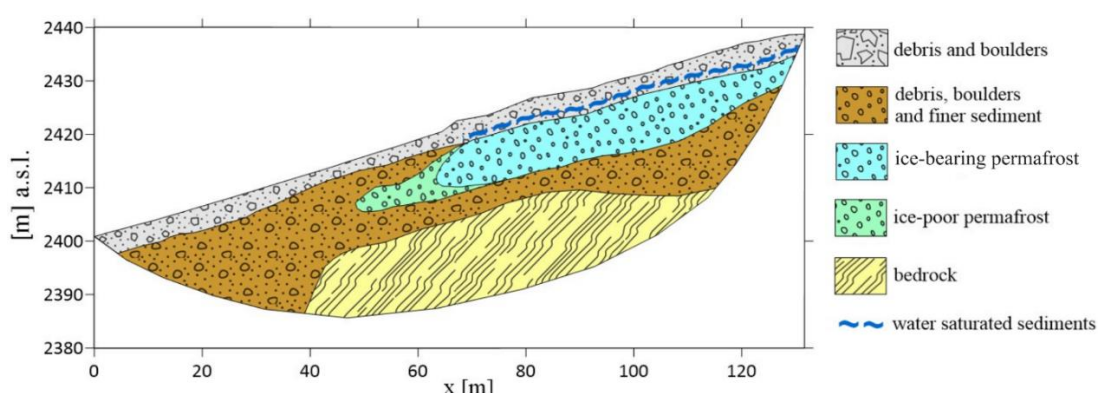
376

377 **Figure 7: (a) Conceptual model used for the synthetic ERT modelling; (b) Synthetic electrical resistivity**  
 378 **model derived from forward modelling applied to the conceptual model presented in Fig. 7a.**

379 **6 Discussion**

380 **6.1 Rock glacier subsurface model and rock glacier hydrology**

381  
 382 Based on our presented ERT, SRT, MASW field data results, and ERT and FW seismic synthetic modelling, we  
 383 constructed a subsurface model of the Flüela rock glacier (Fig. 8).  
 384



385  
 386 **Figure 8: Interpreted subsurface model of the Flüela rock glacier along the geophysical measuring line, derived from**  
 387 **results of Electrical Resistivity Tomography (ERT), Seismic Refraction Tomography (SRT), Multichannel Analysis of**  
 388 **Surface Waves (MASW), and Full-Wave (FW) seismic synthetic modelling.**

389 Four main units were identified. The uppermost layer, showing relatively high resistivity values (20 - 40 kΩm;  
 390 Fig. 2a) and low seismic velocities ( $V_p < 600$  m/s and  $V_s \sim 250$  m/s; Fig. 2b and Figs. 3e-f), was interpreted as

391 mainly composed of debris and blocks, with high porosity (air) and poor regarding fine sediments. The deeper  
392 unfrozen sediment layer, with lower resistivities ( $< 10 \text{ k}\Omega\text{m}$ ) and relatively higher seismic velocities  
393 ( $V_p = 1200 - 1500 \text{ m/s}$  and  $V_s \sim 500 \text{ m/s}$ ), was interpreted as a more heterogeneous compacted layer with both  
394 coarse and fine sediments. At the bottom of the model, the presence of bedrock was hypothesized, considering  
395 the sharp increase of  $V_p$  from 1200 - 1500 m/s to values  $> 3000 \text{ m/s}$  (up to 6000 m/s), and of  $V_s$  values from  
396  $\sim 500 \text{ m/s}$  to  $\sim 2000 \text{ m/s}$  at  $\sim 14 \text{ m}$  depth for the left part of the section, and  $\sim 18 \text{ m}$  depth for the right part.  
397 Considering that MASW applies a 1D approximation, the  $V_p$  model was mainly used to define the bedrock depth  
398 spatially. Finally, the high resistivity values ( $> 80 \text{ k}\Omega\text{m}$ ) identified in the right part of the resistivity model between  
399  $\sim 5 \text{ m}$  and  $\sim 10 \text{ m}$  depth, corresponding to a sharp increase of  $V_s$  values (up to 2000 m/s), were interpreted as an  
400 ice-bearing permafrost layer. It should be noted that the high resistive layer also propagates beyond the middle of  
401 the array ( $50 < x < 65 \text{ m}$ ), but with lower values ( $\sim 40 \text{ k}\Omega\text{m}$ ), probably linked to a decrease in the ice content or  
402 an increase in temperature.

403 Considering that an ice-rich layer typically acts as an aquiclude (Giardino et al., 1992;  
404 Krainer et al., 2007; Pavoni et al., 2023a; Arenson et al., 2022), we hypothesized the presence of a water-saturated  
405 layer above the permafrost. The ice-bearing layer is likely not detected in the  $V_p$  model because of (i) high picking  
406 uncertainties, due to the challenging environment (high level of scattering, wind noise) and (ii) the presence of a  
407 liquid-saturated layer that, in SRT studies, can obstruct energy transmission and mask additional impedance  
408 contrasts at depth (Carcione and Picotti, 2006; Picotti et al., 2007; Shi et al., 2024). This hypothesis can be further  
409 supported by the presence of a thin layer of fine-to-coarse sediments above a thicker, ice-bearing permafrost layer,  
410 as proposed by Boaga et al. (2024). These finer sediments are known to retain more water due to their smaller  
411 particle size, particularly if clay or silt is present (Hillel, 2003). However, without ground truthing, particularly  
412 drilling, we cannot obtain detailed subsurface information to confirm the exact structure and stratigraphy.  
413 Definitive statements regarding the ice and water content or the flow of water within the ice-bearing layer, such  
414 as intra-permafrost flow or the presence of taliks, cannot yet be made. Recent drilling in a rock glacier has revealed  
415 that areas identified as ice-rich using ERT and SRT methods can also contain significant amounts of liquid water  
416 and very fine sediments (personal observations by M. Phillips and A. Bast, SLF, 2024). Combining our methods  
417 with additional techniques could provide further insights into the hydrology of rock glaciers in the future. For  
418 example, Boaga et al. (2020) demonstrated that highly conductive anomalies in the subsurface, detected using  
419 Frequency Domain Electromagnetometry (FDEM) on a rock glacier, can indicate taliks or areas rich in liquid  
420 water.

421

## 422 **6.2 Advancements and challenges in using MASW for rock glacier characterisation**

423

424 Currently, the only two existing examples of MASW used for rock glacier characterisation are those by (i)  
425 Guillemot et al. (2021) at the Laurichard rock glacier, France, and (ii) Kuehn et al. (2024) at the Sourdough Rock  
426 Glacier, Alaska. However, in the first study, MASW was used in combination with other techniques to constrain  
427 a reference model of the unfrozen conditions for mechanical modelling of the rock glacier. In the second study,  
428 the aim of the study was to characterise the first few meters of a debris layer, achieved through a high-resolution  
429 seismic acquisition with sub-metre geophone spacing. Therefore, to our knowledge, the study presented here is  
430 the first successful application of MASW to derive structural information about rock glaciers, particularly

431 concerning the presence of the frozen layer. Indeed, surface wave analysis in periglacial environments is not  
432 straightforward. Surface wave penetration depends on the ability to generate low frequencies, which in turn  
433 requires heavy sources. The logistical constraints due to the high-mountain environments might hinder this  
434 method. Seismic datasets acquired in these contexts are also very noisy due to the scattering produced by debris  
435 and boulders and are highly attenuated, which reflects unclear modal distribution and narrow usable frequency  
436 bands. The mountainous environment may also affect data quality due to harsh weather conditions, particularly  
437 wind, and complex topography. Furthermore, rock glaciers are often highly heterogeneous media that vary  
438 significantly in both space and depth; complex 2D/3D structures could generate dispersion images that are difficult  
439 to interpret, which challenges data processing and interpretation. For this reason, the choice of the spatial window  
440 for the analysis should be made carefully to achieve the best lateral resolution without compromising spectral  
441 resolution. In the case of the Flüela rock glacier, the most natural choice was to perform MASW on the lower and  
442 upper halves of the line due to the relatively homogeneous conditions on each side. At locations with greater  
443 heterogeneity, selecting a suitable window length may be more difficult.

444 **7 Conclusions**

445  
446 In this study, we highlighted the potential limitations of the SRT technique in accurately imaging ice-bearing  
447 layers in high-mountain rock glaciers, a limitation that may also apply to other permafrost environments. This  
448 limitation can be particularly relevant when a supra-permafrost water-saturated layer is present, acting as a  
449 preferential waveguide for seismic refractions and masking the underlying structures. Moreover, in these  
450 environments relatively high travel-time errors can further reduce the visibility of velocity contrasts. Another  
451 well-known limitation of the SRT method is its inability to image velocity inversions in the subsurface, such as  
452 an unfrozen sediment layer between the ice-bearing layer and the bottom bedrock.

453 As shown in our study, the surface wave analysis has the potential to overcome both of these limitations. Surface  
454 waves can be recorded simultaneously with the collection of seismic refraction data as long as low-frequency  
455 geophones are used for the acquisition. The analysis of surface wave dispersion in the frequency-wavenumber (f–  
456 k) spectrum, followed by the inversion of dispersion curves, enables the retrieval of Vs profiles, which are  
457 insensitive to the liquid phase (i.e., they are not affected by the presence of a supra-permafrost water-saturated  
458 layer). Moreover, surface wave dispersion analysis can retrieve velocity inversions with depth and resolve the  
459 presence of a low-velocity layer between high-velocity layers. This method is also less sensitive to random seismic  
460 noise due to scattering and external noise sources, which can interfere with the accurate picking of first-time  
461 arrivals in SRT analysis, providing an alternative and reliable solution for the analysis of seismic datasets affected  
462 by relatively high noise levels. At the Flüela rock glacier, the dispersion images of the left and right sides of the  
463 seismic section look different in terms of frequency content and velocity distribution. The Vs profile produced by  
464 the inversion of the right-side dispersion curve clearly shows an increase of velocities at 5 m depth, attributed to  
465 the ice-bearing layer, and a decrease at about 10 m, compatible with the presence of unfrozen sediments. This  
466 demonstrates the effectiveness of MASW for imaging the ice-bearing layer and the underlying unfrozen  
467 sediments, even in the presence of a supra-permafrost water layer and with a relatively noisy dataset, as well as  
468 the potential to retrieve the thickness of the ice-bearing layer to support the ERT findings.

469 In the future, we plan to implement the MASW technique across various locations, particularly where we have  
470 borehole information on the subsurface stratigraphy, to further validate our findings. Additionally, we aim to  
471 enhance the surface wave analysis by incorporating passive seismic data, such as ambient seismic noise captured  
472 by seismic nodes, to extend our depth of penetration beneath the ice-rich layer to the seismic bedrock.

473 We recommend using low-frequency geophones and appropriate heavy sources whenever possible when  
474 collecting SRT profiles. This approach will enable complementary MASW analysis and provide valuable  
475 experience, which will undoubtedly benefit mountain permafrost research and enhance our understanding of ice  
476 and water content in mountain permafrost, i.e., mountain permafrost hydrology.

477

478 *Data Availability Statement:* The datasets used to obtain the results presented in this work are available at the  
479 open-source repository <https://researchdata.cab.unipd.it/id/eprint/1748>. Furthermore, the ERT datasets will also  
480 be included in the International Database of Geoelectrical Surveys on Permafrost (IDGSP).

481 *Author contribution:* IB and MP developed the concept of the study; MP, JB, and AB collected the data; MP  
482 performed the data processing of ERT and SRT data; IB and SJGT performed the MASW analysis; all authors  
483 contributed to the interpretation of the results, writing and editing of the manuscript.

484 *Competing interests:* The contact author has declared that none of the authors has any competing interests.

485 *Acknowledgements:* The authors want to thank Dr Marcia Phillips for her valuable help and for pre-reviewing the  
486 manuscript.

487

488 *Financial support:* The project “Cold spot” is part of the excellence program: “The Geosciences for Sustainable  
489 Development” project (Budget Ministero dell’Università e della Ricerca - Dipartimenti di Eccellenza 2023–2027  
490 C93C23002690001).

## 491 **References**

492 Arenson, L., Hoelzle, M., and Springman, S.: Borehole deformation measurements and internal structure of some  
493 rock glaciers in Switzerland, *Permafrost and Periglacial Processes*, 13(2), 117–135,  
494 <https://doi.org/10.1002/ppp.414>, 2002.

495 Arenson, L., and Jakob, M.: Periglacial geohazard risks and ground temperature increases, *Eng. Geol. Soc.*  
496 *Territory*, 1, 233–237, [https://doi.org/10.1007/978-3-319-09300-0\\_44](https://doi.org/10.1007/978-3-319-09300-0_44), 2014.

497 Arenson, L.U., and Jakob, M.: Permafrost-related geohazards and infrastructure construction in mountainous  
498 environments, *Oxf. Res. Encycl. Nat. Hazard Sci.*, 30, <https://doi.org/10.1093/acrefore/9780199389407.013.292>,  
499 2017.

500 Arenson, L. U., and Sego, D. C.: The effect of salinity on the freezing of coarse-grained sands, *Can. Geotech. J.*,  
501 43, 325–337, <https://doi.org/10.1139/t06-006>, 2006.

502 Arenson, L. U., Harrington, J. S., Koenig, C. E. M., and Wainstein, P. A.: Mountain Permafrost Hydrology—A  
503 Practical Review Following Studies from the Andes, *Geosciences*, 12, 48,  
504 <https://doi.org/10.3390/geosciences12020048>, 2022.

505 Bast, A., Bründl, M., and Phillips, M.: CCAMM - A research program for studying the impacts of climate change  
506 on mass movements in alpine regions, *Interpraevent 2024. Conference proceedings*, 37–39, 2024a.

507 Bast, A., Kenner, R., and Phillips, M.: Short-term cooling, drying, and deceleration of an ice-rich rock glacier,  
508 The Cryosphere, 18, 3141–3158, <https://doi.org/10.5194/tc-18-3141-2024>, 2024b.

509 Bast, A., Pavoni, M., Lichtenegger, M., Buckel, J., and Boaga, J.: The use of textile electrodes for electrical  
510 resistivity tomography in periglacial, coarse blocky terrain: a comparison with conventional steel electrodes,  
511 Permafrost and Periglacial Processes, 36(1), 110-122, <https://doi.org/10.1002/ppp.2257>, 2025.

512 Bauer, K., Moeck, I., Norden, B., Schulze, A., Weber, M., and Wirth, H.: Tomographic P wave velocity and  
513 vertical velocity gradient structure across the geothermal site Groß Schönebeck (NE German Basin): relationship  
514 to lithology, salt tectonics, and thermal regime, J. Geophys. Res. Solid Earth, 115, B08312,  
515 <https://doi.org/10.1029/2009JB006895>, 2010.

516 Binley, A., and Slater, L.: Resistivity and Induced Polarization: Theory and Practice, Cambridge University Press,  
517 <https://doi.org/10.1017/9781108685955>, 2020.

518 Blanchy, G., Saneiyan, S., Boyd, J., McLachlan, P., and Binley, A.: ResIPy, an intuitive open source software for  
519 complex geoelectrical inversion/modelling, Computers & Geosciences, 137, 104423.  
520 <https://doi.org/10.1016/j.cageo.2020.104423>, 2020.

521 Boaga, J., Cassiani, G., Strobbia, C., and Vignoli, G.: Mode misidentification in Rayleigh waves: Ellipticity as a  
522 cause and a cure. Geophysics 78(4): EN17-EN28, <https://doi.org/10.1190/GEO20120194.1>, 2013.

523 Boaga, J., Phillips, M., Noetzli, J., Haberkorn, A., Kenner, R., and Bast, A.: A comparison of frequency domain  
524 electro-magnetometry, electrical resistivity tomography and borehole temperatures to assess the presence of ice  
525 in a rock glacier, Frontiers in Earth Science, 8, 586430, <https://doi.org/10.3389/feart.2020.586430>, 2020.

526 Boaga, J., Pavoni, M., Bast, A., and Weber, S.: Brief communication: On the potential of seismic polarity reversal  
527 to identify a thin low-velocity layer above a high-velocity layer in ice-rich rock glaciers, The Cryosphere, 18,  
528 3231–3236, <https://doi.org/10.5194/tc-18-3231-2024>, 2024.

529 Bohlen, T., Kugler, S., Klein, G., and Theilen, F.: 1.5D inversion of lateral variation of Scholte-wave dispersion,  
530 Geophysics, 69, 330344, <https://doi.org/10.1190/1.1707052>, 2004.

531 Boiero, D., and Socco, L.V.: The meaning of surface wave dispersion curves in weakly laterally varying  
532 structures, Near Surface Geophysics, 9, 561570, <https://doi.org/10.3997/1873-0604.2011042>, 2011.

533 Bommer, C., Phillips, M., and Arenson, L. U.: Practical recommendations for planning, constructing and  
534 maintaining infrastructure in mountain permafrost, Permafrost and Periglacial Processes, 21, 97–104,  
535 <https://doi.org/10.1002/ppp.679>, 2010.

536 Buckel, J., Mudler, J., Gardeweg, R., Hauck, C., Hilbich, C., Frauenfelder, R., Kneisel, C., Buchelt, S., Blöthe, J.  
537 H., Hördt, A., and Bücker, M.: Identifying mountain permafrost degradation by repeating historical electrical  
538 resistivity tomography (ERT) measurements, The Cryosphere, 17(7), 2919-2940, <https://doi.org/10.5194/tc-17-2919-2023>, 2023.

540 Carcione, J. M., and Picotti, S.: P-wave seismic attenuation by slow-wave diffusion: Effects of inhomogeneous  
541 rock properties, Geophysics, 71(3), O1-O8, <https://doi.org/10.1190/1.2194512>, 2006.

542 Cicora, A., Marcer, M., Gärtner-Roer, I., Bodin, X., Arenson, L. U., and Vieli, A.: A general theory of rock  
543 glacier creep based on in-situ and remote sensing observations, Permafrost and Periglacial Processes, 32(1), 139-  
544 153, <https://doi.org/10.1002/ppp.2090>, 2021.

545 Cicora, A., Beutel, J., Faillettaz, J., and Vieli, A.: Water controls the seasonal rhythm of rock glacier flow, Earth  
546 and Planetary Science Letters, 528, 115844, <https://doi.org/10.1016/j.epsl.2019.115844>, 2019.

547 Colombero, C., Di Toro, L., Khosro Anjom, F., Godio, A., and Morra Di Cella, U.: Ambient Seismic Noise and  
548 Microseismicity Monitoring of Periglacial Bodies: A Case Study on the Gran Sometta Rock Glacier (NW Italian  
549 Alps), Permafrost and Periglacial Processes, 0:1–16, <https://doi.org/10.1002/ppp.22862025>, 2025.

550 Day-Lewis, F. D., Johnson, C. D., Singha, K., Lane, J.W.J.: Best practices in electrical resistivity imaging: Data  
551 collection and processing, and application to data from Corinna, Maine, EPA Report, Boston, MA, 2008.

552 De Pasquale, G., Valois, R., Schaffer, N., and MacDonell, S.: Contrasting geophysical signatures of a relict and  
553 an intact Andean rock glacier, *The Cryosphere*, 16(5), 1579-1596, <https://doi.org/10.5194/tc-16-1579-2022>, 2022.

554 Duvillard, P. A., Ravanel, L., Marcer, M., and Schoeneich, P.: Recent evolution of damage to infrastructure on  
555 permafrost in the French Alps, *Reg. Environ. Change*, 19 (5), 1281–1293, <https://doi.org/10.1007/s10113-019-01465-z>, 2019.

557 Everett, M. E.: *Near-Surface Applied Geophysics*. Cambridge University Press,  
558 <https://doi.org/10.1017/CBO9781139088435>, 2013.

559 Foti, S., Lai, C. G., Rix, G. J., and Strobbia, C.: Surface wave methods for near-surface site characterization, CRC  
560 Press, ISBN: 9781138077737, 2015.

561 Giardino, J.R., Vitek, J.D., and Demorett, J.L.: A model of water movement in rock glaciers and associated water  
562 characteristics, in: *Periglacial Geomorphology*, edited by: Dixon, J.C., and Abrahams, A.D., Routledge, London,  
563 159-184, <https://doi.org/10.4324/9781003028901-7>, 1992.

564 Glazer, M., Dobiński, W., Marciniak, A., Majdański, M., and Błaszczyk, M.: Spatial distribution and controls of  
565 permafrost development in non-glacial Arctic catchment over the Holocene, *Fuglebekken, SW Spitsbergen,*  
566 *Geomorphology*, 358, 107128, <https://doi.org/10.1016/j.geomorph.2020>, 2020.

567 Guillemot, A., Helmstetter, A., Larose, E., Baillet, L., Garambois, S., Mayoraz, R., and Delaloye, R.: Seismic  
568 monitoring in the Gugla rock glacier (Switzerland): ambient noise correlation, microseismicity and modeling,  
569 *Geophysical Journal International*, 221 (3), 1719-1735, <https://doi.org/10.1093/gji/ggaa097>, 2020.

570 Guillemot, A., Baillet, L., Garambois, S., Bodin, X., Helmstetter, A., Mayoraz, R., and Larose, E.: Modal  
571 sensitivity of rock glaciers to elastic changes from spectral seismic noise monitoring and modelling, *The*  
572 *Cryosphere*, 15, 501–529, <https://doi.org/10.5194/tc-15-501-2021>, 2021.

573 Haeberli, W.: Untersuchungen zur Verbreitung von Permafrost zwischen Flüelapass und Piz Graletsch  
574 (Graubünden), *Mitteilung der Versuchsanstalt für Wasserbau, Hydrologie und Glaziologie*, ETH Zurich, Zurich,  
575 1975.

576 Haeberli, W., Kääb, A., Wagner, S., Mühl, D. V., Geissler, P., Haas, J. N., ... and Wagenbach, D.: Pollen analysis  
577 and 14C age of moss remains in a permafrost core recovered from the active rock glacier Murtèl-Corvatsch, Swiss  
578 Alps: geomorphological and glaciological implications, *Journal of Glaciology*, 45(149), 1-8,  
579 <https://doi.org/10.3189/S002214300002975>, 1999.

580 Haeberli, W., Hallet, B., Arenson, L., Elconin, R., Humlum, O., Kääb, A., and Mühl, D. V.: Permafrost creep  
581 and rock glacier dynamics, *Permafrost and Periglacial Processes*, 17(3), 189-214, <https://doi.org/10.1002/ppp.561>,  
582 2006.

583 Hauck, C.: Frozen ground monitoring using DC resistivity tomography, *Geophysical Research Letters*, 29(21),  
584 12-1-12-4, <https://doi.org/10.1029/2002GL014995>, 2002.

585 Hauck, C., & Vonder Mühl, D.: Detecting seasonal changes in permafrost using geophysical methods, *Permafrost*  
586 and *Periglacial Processes*, 14(3), 213–222, <https://doi.org/10.1002/ppp.451>, 2003.

587 Hauck, C., and Kneisel, C.: *Applied Geophysics in Periglacial Environments*, Cambridge University Press., 2008.

588 Hauck, C., Böttcher, M., and Maurer, H.: A new model for estimating subsurface ice content based on combined  
589 electrical and seismic data sets, *The Cryosphere*, 5, 453–468, <https://doi.org/10.5194/tc-5-453-2011>, 2011.

590 Herrmann, R. B.: *Computer Programs in Seismology*, St Louis University, 1987.

591 Hilbich, C., Fuss, C., Mollaret, C., Hauck, C., and Hoelzle, M.: Multi-decadal geophysical monitoring of  
592 permafrost evolution in mountain terrain – The PACE legacy, *The Cryosphere*, 15(11), 5121–5145,  
593 <https://doi.org/10.5194/tc-15-5121-2021>, 2021.

594 Hu, Y., Arenson, L. U., Barboux, C., Bodin, X., Cicoira, A., Delaloye, R., Gärtner-Roer, I., Kääb, A., Kellerer-  
595 Pirklbauer, A., Lambiel, C., Liu, L., Pellet, C., Rouyet, L., Schoeneich, P., Seier, G., and Strozzi, T.: Rock Glacier  
596 Velocity: An Essential Climate Variable Quantity for Permafrost, *Reviews of Geophysics*, 63, e2024RG000847,  
597 <https://doi.org/10.1029/2024RG000847>, 2025.

598 Janke, J.R., Regmi, N.R., Giardino, J.R., and Vitek, J.D.: Rock glaciers, in: *Treatise on Geomorphology*, Elsevier  
599 Inc., Amsterdam, The Netherlands, 238–273, <https://doi.org/10.1016/B978-0-444-63369-9.00012-4>, 2013.

600 Jacquemart, M., Weber, S., Chiarle, M., Chmiel, M., Cicoira, A., Corona, C., Eckert, N., Gaume, J., Giacoma, F.,  
601 Hirschberg, J., Kaitna, R., Magnin, F., Mayer, S., Moos, C., van Herwijnen, A., and Stoffel, M.: Detecting the  
602 impact of climate change on alpine mass movements in observational records from the European Alps, *Earth-  
603 Science Reviews*, 258, 104886, <https://doi.org/10.1016/j.earscirev.2024.104886>, 2024.

604 Jones, D. B., Harrison, S., Anderson, K., and Whalley, W. B.: Rock glaciers and mountain hydrology: A review,  
605 *Earth-Science Reviews*, 193, 66–90, <https://doi.org/10.1016/j.earscirev.2019.04.001>, 2019.

606 Kellerer-Pirklbauer, A., Bodin, X., Delaloye, R., Lambiel, C., Gärtner-Roer, I., Bonnefoy-Demongeot, M., ... and  
607 Zumiani, M.: Acceleration and interannual variability of creep rates in mountain permafrost landforms (rock  
608 glacier velocities) in the European Alps in 1995–2022, *Environmental Research Letters*, 19(3), 034022,  
609 <https://doi.org/10.1088/1748-9326/ad25a4>, 2024.

610 Kenner, R., Phillips, M., Hauck, C., Hilbich, C., Mulsow, C., Bühler, Y., ... and Buchroithner, M.: New insights  
611 on permafrost genesis and conservation in talus slopes based on observations at Flüelapass, Eastern Switzerland,  
612 *Geomorphology*, 290, 101-113, <https://doi.org/10.1016/j.geomorph.2017.04.011>, 2017.

613 Kenner, R., Noetzli, J., Hoelzle, M., Raetzo, H., and Phillips, M.: Distinguishing ice-rich and ice-poor permafrost  
614 to map ground temperatures and ground ice occurrence in the Swiss Alps. *The Cryosphere*, 13(7), 1925–1941,  
615 <https://doi.org/10.5194/tc-13-1925-2019>, 2019.

616 Kenner, R., Pruessner, L., Beutel, J., Limpach, P., and Phillips, M.: How rock glacier hydrology, deformation  
617 velocities and ground temperatures interact: Examples from the Swiss Alps, *Permafrost Periglac*, 31, 3–14,  
618 <https://doi.org/10.1002/ppp.2023>, 2020.

619 Kofler, C., Mair, V., Gruber, S., Todisco, M. C., Nettleton, I., Steger, S., ... and Comiti, F.: When do rock glacier  
620 fronts fail? Insights from two case studies in South Tyrol (Italian Alps), *Earth Surface Processes and Landforms*,  
621 46(7), 1311–1327, <https://doi.org/10.1002/esp.5099>, 2021.

622 Krainer, K. and Mostler, W.: Hydrology of Active Rock Glaciers: Examples from the Austrian Alps, Arctic,  
623 Antarctic, and Alpine Research, 34, 142–149, <https://doi.org/10.1080/15230430.2002.12003478>, 2002.

624 Krainer, K., Mostler, W., and Spötl, C.: Discharge from active rock glaciers, Austrian Alps: a stable isotope  
625 approach, *Austrian Journal of Earth Sciences*, 100, 102–112, 2007.

626 Krainer, K., Bressan, D., Dietre, B., Haas, J. N., Hajdas, I., Lang, K., ... and Tonidandel, D.: A 10,300-year-old  
627 permafrost core from the active rock glacier Lazaun, southern Ötztal Alps (South Tyrol, northern Italy),  
628 *Quaternary Research*, 83(2), 324–335, <https://doi.org/10.1016/j.yqres.2014.12.005>, 2015.

629 Kuehn, T., Holt, J. W., Johnson, R., and Meng, T.: Active seismic refraction, reflection, and surface wave surveys  
630 in thick debris-covered glacial environments, *Journal of Geophysical Research: Earth Surface*, 129,  
631 <https://doi.org/10.1029/2023JF007304>, 2024.

632 Kula, D., Olszewska, D., Dobrowski, W., and Glazer, M.: Horizontal-to-vertical spectral ratio variability in the  
633 presence of permafrost, *Geophysical Journal International*, 214, 219–231, <https://doi.org/10.1093/gji/ggy118>,  
634 2018.

635 Lerjen, M., Kääb, A., Hoelzle, M., and Haeberli, W.: Local distribution pattern of discontinuous mountain  
636 permafrost. a process study at Flüela Pass, Swiss Alps, in: Proceedings of the 8th International Conference on  
637 Permafrost, Zurich, Switzerland, 667-672, ISBN: 90 5809 582 7, 2003.

638 Liu, H., Maghoul, P., and Shalaby, A.: Seismic physics-based characterization of permafrost sites using surface  
639 waves, *The Cryosphere*, 16, 1157–1180, <https://doi.org/10.5194/tc-16-1157-2022>, 2022.

640 Mair, V., Zischg, A., Lang, K., Tonidandel, D., Krainer, K., Kellerer-Pirklbauer, A., ... and Böckli, L.: PermaNET-  
641 Permafrost Long-term Monitoring Network. Synthesis report (Vol. 1), International Research Society  
642 INTERPRAEVENT, ISBN 978-3-901164-14-9, 2011.

643 Noetzli, J., Isaksen, K., Barnett, J., Christiansen, H. H., Delaloye, R., Etzelmüller, B., ... and Phillips, M.: Enhanced warming of European mountain permafrost in the early 21st century, *Nature Communications*, 15(1),  
644 1-15, <https://doi.org/10.1038/s41467-024-54831-9>, 2024.

645 Olafsdottir, E. A., Bessason, B., Erlingsson, S., and Kaynia, A. M.: A Tool for Processing and Inversion of MASW  
646 Data and a Study of Inter-session Variability of MASW, *Geotechnical Testing Journal*, 47(5), 1006-1025,  
647 <https://doi.org/10.1520/GTJ20230380>, 2024.

648 Park, C. B., Miller, R. D., and Xia, J.: Multichannel analysis of surface waves, *Geophysics*, 64(3), 800808,  
649 <https://doi.org/10.1190/1.1444590>, 1999.

650 Park, C. B., Miller, R. D., Xia, J., and Ivanov, J.: Multichannel analysis of surface waves (MASW) - active and  
651 passive methods, *The Leading Edge*, 26(1), 60-64, <https://doi.org/10.1190/1.2431832>, 2007.

652 Park, C., Richter, J., Rodrigues, R., and Cirone, A.: MASW applications for road construction and maintenance,  
653 *The Leading Edge*, 37(10), 724-730, <https://doi.org/10.1190/tle37100724.1>, 2018.

654 Pavoni, M., Carrera, A., and Boaga, J.: Improving the galvanic contact resistance for geoelectrical measurements  
655 in debris areas: A case study, *Near Surface Geophysics*, 20(2), 178-191, <https://doi.org/10.1002/nsg.12192>, 2022.

656 Pavoni, M., Boaga, J., Carrera, A., Zuecco, G., Carturan, L., and Zumiani, M.: Brief communication: Mountain  
657 permafrost acts as an aquitard during an infiltration experiment monitored with electrical resistivity tomography  
658 time-lapse measurements, *The Cryosphere*, 17, 1601–1607, <https://doi.org/10.5194/tc-17-1601-2023>, 2023a.

659 Pavoni, M., Boaga, J., Wagner, F. M., Bast, A., and Phillips, M.: Characterization of rock glaciers environments  
660 combining structurally-coupled and petrophysically-coupled joint inversions of electrical resistivity and seismic  
661 refraction datasets, *Journal of Applied Geophysics*, 215, 105097, <https://doi.org/10.1016/j.jappgeo.2023.105097>,  
662 2023b.

663 Petersson, N.A., and Sjögren, B.: User's guide to SW4, version 3.0, LLNL-SM-741439 (LLNL-SM-741439),  
664 2023.

665 PERMOS 2020: Swiss Permafrost Bulletin 2018/2019. Pellet, C. and Noetzli, J. (eds.), 20 pp.,  
666 [doi.org/10.13093/permos-bull-2020](https://doi.org/10.13093/permos-bull-2020), 2020.

667 Phillips, M., Mutter, E. Z., Kern-Luetschg, M., and Lehning, M.: Rapid degradation of ground ice in a ventilated  
668 talus slope: Flüela Pass, Swiss Alps, *Permafrost Periglac.*, 20, 1–14, <https://doi.org/10.1002/ppp.638>, 2009.

669 Phillips, M., Buchli, C., Weber, S., Boaga, J., Pavoni, M., and Bast, A.: Brief communication: Combining  
670 borehole temperature, borehole piezometer and cross-borehole electrical resistivity tomography measurements to  
671 investigate seasonal changes in ice-rich mountain permafrost, *The Cryosphere*, 17, 753–760,  
672 <https://doi.org/10.5194/tc-17-753-2023>, 2023.

673 Picotti, S., Carcione, J. M., Germán Rubino, J., and Santos, J. E.: P-wave seismic attenuation by slow-wave  
674 diffusion: Numerical experiments in partially saturated rocks, *Geophysics*, 72(4), N11-N21,  
675 <https://doi.org/10.1190/1.2740666>, 2007.

676 Pride, S.R., Berryman, J.G., and Harris, J.M.: Seismic attenuation due to wave-induced flow, *Journal of  
677 Geophysical Research*, 109, B01201, <https://doi.org/10.1029/2003JB002639>, 2004.

678

679 RGIK. Towards standard guidelines for inventorying rock glaciers: baseline concepts (version 4.2.2), IPA Action  
680 Group Rock glacier inventories and kinematics, 13 pp, 2022.

681 Rücker, C., Günther, T., and Wagner, F. M.: pyGIMLi: An open-source library for modelling and inversion in  
682 geophysics, *Computers & Geosciences*, 109, 106-123, <https://doi.org/10.1016/j.cageo.2017.07.011>, 2017.

683 Sambridge, M.: Geophysical inversion with a neighbourhood algorithm: I. Searching a parameter space,  
684 *Geophysical Journal International*, 138(2), 479–494, <https://doi.org/10.1046/j.1365-246X.1999.00876.x>, 1999.

685 Scott, W. J., Sellmann, P., and Hunter, J. A.: Geophysics in the study of permafrost, *Geotechnical and*  
686 *environmental geophysics*, 1, 355-384, <https://doi.org/10.1190/1.9781560802785.ch13>, 1990.

687 Shi Z., He X., Chen D., and Wang X.: Seismic wave dispersion and attenuation resulting from multiscale wave-  
688 induced fluid flow in partially saturated porous media, *Geophysical Journal International*, 236, 1172–1182,  
689 <https://doi.org/10.1093/gji/ggad475>, 2024.

690 Sjögreen, B., and Petersson, N.A.: A Fourth Order Accurate Finite Difference Scheme for the Elastic Wave  
691 Equation in Second Order Formulation, *Journal of Scientific Computing*, 52(1), 17-48,  
692 <https://doi.org/10.1007/s10915-011-9531-1>, 2012.

693 Socco, L. V., Foti, S. and Boiero, D.: Surface-wave analysis for building near-surface velocity models -  
694 Established approaches and new perspectives, *Geophysics*, 75(5), 75A83–75A102,  
695 <https://doi.org/10.1190/1.3479491>, 2010.

696 Tourei, A., Ji, X., Rocha dos Santos, G., Czarny, R., Rybakov, S., Wang, Z., Hallissey, M., Martin, E. R., Xiao  
697 M., Zhu, T., Nicolsky, D., and Jensen, A.: Mapping Permafrost Variability and Degradation Using Seismic  
698 Surface Waves, Electrical Resistivity, and Temperature Sensing: A Case Study in Arctic Alaska, *Journal of*  
699 *Geophysical Research: Earth Surface*, 129, e2023JF007352, <https://doi.org/10.1029/2023JF007352>,  
700 2024.

701 Wagner, F.M., Mollaret, C., Günther, T., Kemna, A., and Hauck, C.: Quantitative imaging of water, ice and air in  
702 permafrost systems through petrophysical joint inversion of seismic refraction and electrical resistivity data,  
703 *Geophys. J. Int.*, 219(3), 1866–1875, <https://doi.org/10.1093/gji/ggz402>, 2019.

704 Wathelet, M., Jongmans D., and Ohrnberger, M.: Surface-wave inversion using a direct search algorithm and its  
705 application to ambient vibration measurements, *Near Surface Geophysics*, 2(4), 211-221,  
706 <https://doi.org/10.3997/1873-0604.2004018>, 2004.

707 Wathelet, M.: An improved neighborhood algorithm: Parameter conditions and dynamic scaling, *Geophysical*  
708 *Research Letters*, 35(9), L09301, <https://doi.org/10.1029/2008GL033256>, 2008.

709 Williams, P. J.: Unfrozen Water Content of Frozen Soils and Soil Moisture Suction, *Géotechnique*, 14, 231–246,  
710 <https://doi.org/10.1680/geot.1964.14.3.231>, 1964.

711 Zhang, L., Wang, S., and Petersson, N.A.: Elastic Wave Propagation in Curvilinear Coordinates with Mesh  
712 Refinement Interfaces by a Fourth Order Finite Difference Method, *SIAM J. Sci. Comp.*, 43(2), A1472-A1496,  
713 <https://doi.org/10.1137/20M1339702>, 2021.